

In vivo targeting of cell death using a synthetic fluorescent molecular probe

Bryan A. Smith · Shuzhang Xiao · William Wolter ·
James Wheeler · Mark A. Suckow ·
Bradley D. Smith

© Springer Science+Business Media, LLC 2011

Abstract A synthetic, near-infrared, fluorescent probe, named PSS-794 was assessed for its ability to detect cell death in two animal models. The molecular probe contains a zinc(II)-dipicolylamine (Zn^{2+} -DPA) affinity ligand that selectively targets exposed phosphatidylserine on the surface of dead and dying cells. The first animal model used rats that were treated with dexamethasone to induce thymic atrophy. Ex vivo fluorescence imaging and histological analysis of excised organs showed thymus uptake of PSS-794 was four times higher than a control fluorophore that lacked the Zn^{2+} -DPA affinity ligand. In addition, the presence of PSS-794 produced a delayed and higher build up of dead and dying cells in the rat thymus. The second animal model employed focal beam radiation to induce cell death in tumor-bearing rats. Whole-body and ex vivo imaging showed that the amount of PSS-794 in a radiation-treated tumor was almost twice that in a non-treated tumor. The results indicate that PSS-794 may be useful for pre-clinical optical detection of tumor cell death due to therapy.

Keywords Cell death · Tumor therapy · Optical imaging · Zinc(II)-dipicolylamine · Molecular probe

B. A. Smith · S. Xiao · B. D. Smith (✉)
Department of Chemistry and Biochemistry, University of Notre
Dame, 236 Nieuwland Science Hall, Notre Dame,
IN 46556, USA
e-mail: smith.115@nd.edu

W. Wolter · M. A. Suckow
Freimann Life Science Center, 400 Galvin Life Science,
University of Notre Dame, Notre Dame, IN 46556, USA

J. Wheeler
Center for Cancer Care, Goshen Health System, 200 High Park
Ave, Goshen, IN 46526, USA

Introduction

The plasma membrane of healthy mammalian cells has an asymmetric distribution of polar lipids. The membrane outer leaflet is comprised primarily of the zwitterionic phospholipids, phosphatidylcholine and sphingomyelin, and thus the exterior membrane surface is close to charge-neutral. The major anionic phospholipid in the plasma membrane is phosphatidylserine (PS) (2–10% of total phospholipid) and it is sequestered almost completely within the membrane inner leaflet by energy consuming ATPase transport processes [1]. Loss of this asymmetric distribution during cell death, cell activation or cell transformation, leads to PS exposure and the cell surface becoming anionic [2, 3]. The last decade has seen mounting evidence that molecular targeting of cells with exposed PS is a broadly effective strategy for diagnosis and treatment of many human diseases [4–7]. Molecules and particles that selectively target anionic cell membrane surfaces with exposed PS and distinguish them from the near-neutral membrane surfaces of normal human cells are currently under extensive investigation as imaging probes, drug delivery agents, and targeted molecular therapeutics [8–15].

Most work with PS targeting agents is focused on imaging cell death. The appearance of PS on the cell surface is a universal indicator of most, if not all, types of cell death [16–20]. Medical fields that have recently conducted preclinical or clinical trials of cell death imaging using molecular probes for exposed PS, include oncology, cardiology, vascular medicine, orthopedics, organ transplantation, gastroenterology, neurology, ophthalmology, autoimmune diseases, and metabolic diseases [21]. The imaging probe in most of these studies is a labeled form of Annexin V, a 36 kDa, single-stranded protein that binds in a Ca^{2+} -dependent manner to membranes that expose anionic phospholipids, including PS [22]. Fluorescently

labeled versions of Annexin V are commonly used in cell biology research for detecting apoptotic cells. Most of the effort to develop Annexin V probes for *in vivo* imaging has employed radioactive derivatives for PET and SPECT modalities [23–25]. While many reports show promising results, clear demonstrations of robust *in vivo* utility remain elusive, and this may be due to potential performance limitations with Annexin V such as extended residence time in the kidneys, biodegradation of the protein, and variable degrees of targeting within a single cohort [26, 27]. Imaging cell death has the additional complication that it is a time dependent process; a high contrast image must be achieved within a specific window in time that in turn depends on the specifics of the cell death phenomenon under study. Therefore, a single cell death probe will not likely be applicable for all types of imaging applications. A more realistic scenario is a palette of related cell death imaging probes with a range of blood clearance rates and different biodistribution patterns.

With a goal of finding imaging probes that are alternatives to Annexin V, investigators have examined other PS-binding proteins such as Annexin VI, Lactadherin and Synaptotagmin-I [28–30]. A refinement of this approach is to create a probe from the PS-binding region of the protein. For example, a fluorescently labeled version of the C2A domain from Synaptotagmin-I (molecular weight 14 kDa) has been shown to detect similar amounts of cell death as an analogous Annexin V derivative [31]. Compared to proteins, it is much easier to systematically fine-tune the pharmacokinetic properties of small molecules, and recently, several independent research groups have employed phage panning technology to identify small peptides (hexamers to decamers) that bind exposed PS with nanomolar dissociation constants [8, 32–35]. Our research group has pioneered an alternative approach using synthetic zinc(II)-dipicolylamine (Zn^{2+} -DPA) coordination complexes, which can selectively recognize anionic membranes over the near-neutral charge membranes of healthy cells [36]. The membrane association process utilizes a three-component assembly process where Zn^{2+} ions mediate cooperative association of the DPA molecule to the anionic head groups of the membrane-bound PS [37, 38]. Functionally, this is similar to the way that Ca^{2+} ions promote membrane association of Annexin V [39–41]. Initial work with fluorescently labeled Zn^{2+} -DPA probes focused on *in vitro* studies using cell culture, but more recently we have developed a version called PSS-794 (Fig. 1), which has an appended near-infrared fluorophore that is suitable for *in vivo* whole-body imaging of small animals [42, 43]. Using this probe we have successfully imaged the dead and dying tissue within rodent models of xenograft tumors and acute muscle damage [44, 45]. Here, we assess the targeting properties of PSS-794 in two

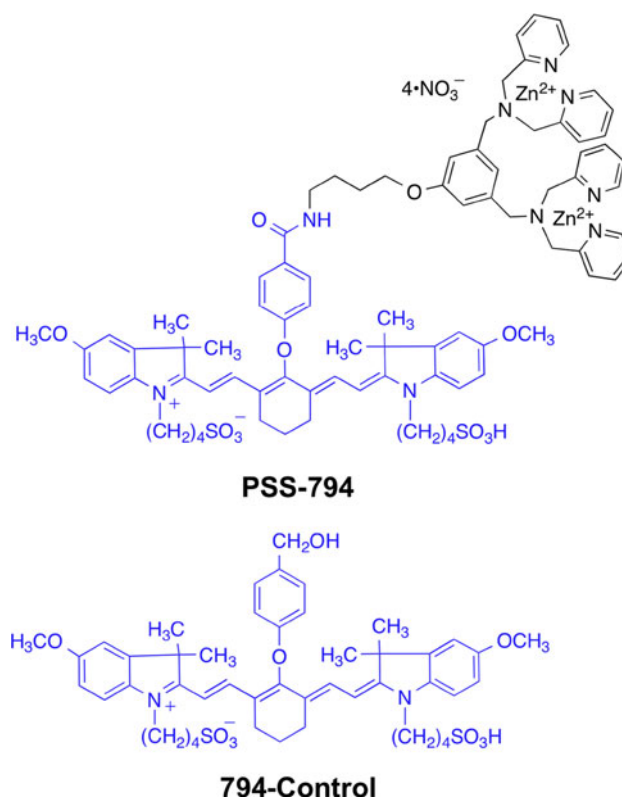


Fig. 1 Chemical structures of PSS-794 and 794-Control

additional rodent models of *in vivo* cell death. We describe studies that employ a well-established thymic atrophy model and we also provide evidence that PSS-794 can detect an increase in tumor cell death due to successful treatment by focal beam radiation.

Materials and methods

Probe synthesis

The synthesis of fluorescent probes, PSS-794 and 794-Control, have been reported previously [42].

Rat model of dexamethasone-induced thymocyte cell death

All animal procedures were approved by the University of Notre Dame Institutional Animal Care and Use Committee. Six cohorts of 8-week old male Lobund-Wistar rats (Freimann Life Science Center, 250 g) ($n = 4$) were given intraperitoneal injections (50 mg/kg) of water soluble dexamethasone (Sigma-Aldrich, St. Louis, MO) dissolved in 400 μ l of distilled H_2O . The time from dexamethasone dosing to sacrifice of the cohort (and its related control cohort) was either 30, 42, or 48 h, with injection of

fluorescent probe at 24 h before sacrifice. The fluorescent probe (either PSS-794 in 1% DMSO/H₂O or 794-Control in H₂O) was injected intravenously via the tail vein and produced a dosage of 3.0 mg/kg. Two additional cohorts of rats ($n = 4$) were not treated with dexamethasone, but were injected with fluorescent probe (either PSS-794 in 1% DMSO/H₂O or 794-Control in H₂O). To evaluate the ability of PSS-794 to detect different levels of thymocyte cell death, three cohorts of rats ($n = 4$) were treated with 10, 25, or 50 mg/kg of dexamethasone. 18 h later, the rats were injected intravenously with PSS-794 (3.0 mg/kg) and sacrificed after another 24 h. Two cohorts of rats ($n = 4$) were used to measure the effect of PSS-794 on the basal level of thymocyte cell death. The rats were not treated with dexamethasone but one cohort was injected intravenously with PSS-794 (3.0 mg/kg). 24 h later both cohorts were sacrificed and the excised thymus from each animal was evaluated by a caspase-3 histology assay. All animals were euthanized by either CO₂ asphyxiation or cervical dislocation under anesthesia.

Detecting increased tumor cell death due to radiation treatment

The right and left rear flanks of eight-week old male Lobund Wistar rats (Freimann Life Science Center, 250 g, $n = 5$) were injected subcutaneously with 1×10^6 rat Prostate Adenocarcinoma III (PAIII) cells, suspended in 300 μ l of Dulbecco's Modified Eagle Medium. 6 days later the tumor-bearing rats were anesthetized with an intraperitoneal injection of a ketamine/xylazine (75/10 mg/kg) cocktail (our previous study of this rat tumor model, only allowed tumor growth for 14 days [44]). The rats were then placed on their left side, and the right flank tumor irradiated with a 3.0 cm diameter beam (20 Gy dose of 9 MeV electrons) produced by a clinical Varian 21 EX accelerator (Varian Medical Systems Inc., Palo Alto, CA). Fur from the animal's lower region was shaved, and the rats were injected intravenously via the tail vein with PSS-794 (3.0 mg/kg) or 794-Control (3.0 mg/kg) at 17 h post-radiation treatment. 24 h later the live rats were anesthetized (1.5% isoflurane inhalation) and subjected to whole-body, epifluorescence imaging. Immediately after live animal imaging, each rat was euthanized and imaged again with the skin removed from the lower region to improve signal intensity at the tumors.

Ex vivo fluorescence imaging

After sacrifice and imaging, selected rat tissues were excised, placed on a transparent imaging tray, and imaged using a Kodak In Vivo Multispectral Imaging System

FX equipped with a 750 ± 10 nm excitation filter and 830 ± 20 nm emission filter (30 s time acquisition, bin = 2×2 , f -stop = 2.51, field of view = 190 mm).

Image analysis

Images were analyzed using *Image J 1.43 m*. The 16-bit images were imported, opened in sequential order, and converted to an image stack. Background subtraction was applied to the images using the rolling ball algorithm (radius = 1000 pixels). The stack was then converted to a montage and pseudocolored as "Thai" (under the "Lookup Tables" menu). Region of interest (ROI) analysis was performed on each ex vivo image by manually drawing an ROI to outline each tissue. The mean pixel intensities for each tissue were measured and recorded. The resulting ROI values were plotted using *Graphpad Prism 4*.

Histology

For each animal, the thymus was excised, flash frozen in OCT compound and sliced at 10 μ m thickness. The sections were incubated overnight with a rabbit anti-human polyclonal caspase-3 antibody (Abcam Inc.; 1:50). The sections were incubated with goat anti-rabbit IgG conjugated to Alexa-Fluor 488 (Invitrogen; 1:500) for 15 min, and then counterstained with DAPI. Fluorescence images of the sections were acquired using a Nikon TE-2000 U epifluorescence microscope equipped with the appropriate UV (ex. 340/80 nm, em. 435/85 nm), GFP (ex. 450/90 nm, em. 500/50 nm), and Cy7 filters (ex. 710/75 nm, em. 810/90 nm). Images were captured using Metamorph software (Universal) and analyzed using *ImageJ 1.43 m*. The caspase-3 levels in Figs. 4 and 5 were determined by averaging the integrated fluorescence in the GFP channel for eight fields of view chosen at random.

Statistical analysis

Results are depicted as mean \pm standard error of the mean (SEM). Statistical analysis was performed using a Student's t -test.

Results

Detection of rat thymocyte cell death using PSS-794

Separate cohorts of rats ($n = 4$) were treated with intraperitoneal injections of dexamethasone (50 mg/kg) to induce thymocyte cell death. The time from dexamethasone treatment to sacrifice for each cohort (and its control cohort) was either 30, 42, or 48 h, with injection of

fluorescent probe (3.0 mg/kg of PSS-794 or 794-Control) at 24 h before sacrifice. These conditions of moderately high probe dose (3.0 mg/kg) and relatively long waiting period after probe injection (24 h) were chosen to ensure maximum uptake at the sites of cell death and complete wash out of any transient, non-targeted, tissue retention effect. The excised internal organs and tissues were imaged using a planar, whole-body epifluorescence scanner with a near-infrared filter set (ex. 750 ± 10 nm, em. 830 ± 20 nm). ROI analysis produced a pixel intensity map of each excised thymus and allowed calculation of mean pixel intensity (MPI). The chromophores in PSS-794 and 794-Control have essentially the same near-infrared absorption/emission wavelengths, so the relative amount of probe in each thymus could be determined by direct comparison of the MPIs. As seen in Fig. 2a, uptake of PSS-794 in the dexamethasone-treated thymi was significantly higher than 794-Control at all time points, and the highest amount of PSS-794 accumulation occurred at 42 h after dexamethasone treatment. Uptake of PSS-794 was also higher than 794-Control in the thymi taken from control rats that were not treated with dexamethasone, which is attributed to PSS-794 targeting the basal cell death in the organ. The data in Fig. 2b shows that PSS-794 accumulation in the thymi increased with size of dexamethasone dosage, showing that probe uptake reflects the degree of thymic atrophy.

Independent confirmation that PSS-794 targets the dead and dying cells within the thymus, was gained from fluorescent histological analyses of excised thymus tissue. Each thymus was flash frozen in the tissue embedding

material OCT, sliced into 10 μ m thick sections and stained with an anti-caspase-3 antibody and DAPI. Thymus sections from rats that were treated with dexamethasone showed a much stronger caspase-3 signal than sections from non-treated rats, indicating increased amounts of cell death (Fig. 3). Near-infrared fluorescence microscopy of the same tissues showed that PSS-794 stained only the regions of tissue that were high in caspase-3 expression (Fig. 3a). In comparison, there was very little uptake of 794-Control in essentially identical thymus tissue sections with high apoptotic index (Fig. 3b).

The PSS-794 targeting data in Fig. 2a suggests that the number of dead and dying thymocytes reached a maximum at 42 h after dexamethasone treatment. This conclusion is consistent with the histology data in Fig. 4b showing that the expression of caspase-3 in thymi from rats treated with both dexamethasone and PSS-794 also peaked at the same time point. The caspase-3 histology data in Fig. 4a corresponds to an experiment that treated a cohort of rats with dexamethasone but did not dose with PSS-794. In this case, the number of dead and dying thymocytes reached a maximum at 12 h after dexamethasone treatment, an earlier time point that agrees with previous studies of this thymocyte cell death model [46]. Figure 5 shows a comparison of caspase-3 histology data for two cohorts of rats that were not treated with dexamethasone but one cohort was dosed with PSS-794. The amount of caspase-3 was 50% higher in the thymus tissues from the rats dosed with PSS-794. The data in Figs. 4 and 5 indicate that the presence of PSS-794 induces a delayed and higher build up of dead and dying cells in the rat thymus.

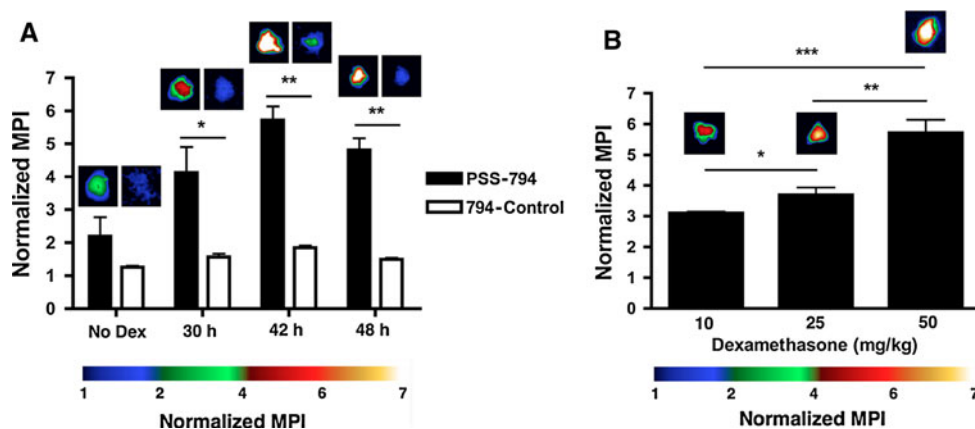
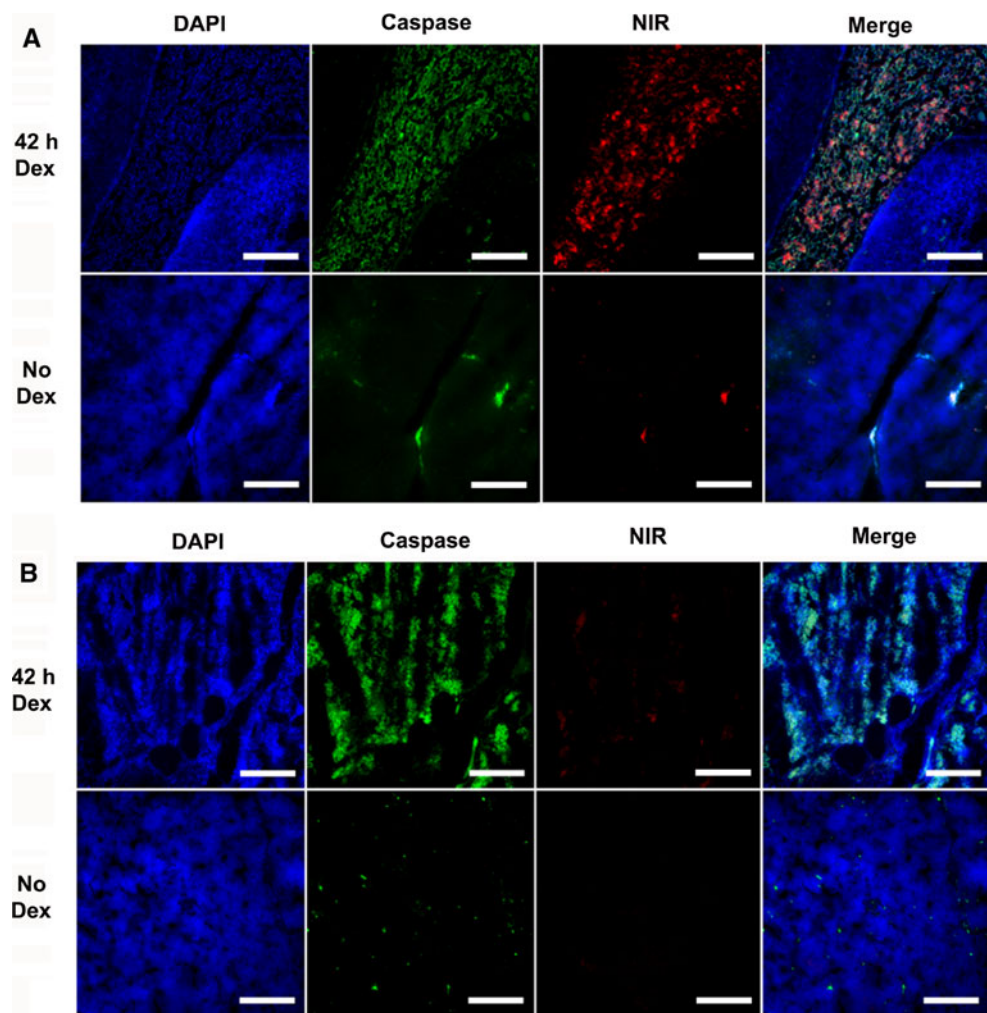


Fig. 2 PSS-794 selectively targets thymocyte cell death in dexamethasone-treated rats. **a** Mean pixel intensities (MPI) of excised thymi from rats that were treated with dexamethasone (50 mg/kg) and dosed with either PSS-794 or 794-Control (3.0 mg/kg). The times indicate the period from dexamethasone treatment to sacrifice and include injection of the fluorescent probe at 24 h before sacrifice. Rats not treated with dexamethasone (No Dex) were dosed with either PSS-794 or 794-Control (3.0 mg/kg) and sacrificed 24 h later. In each

case, the MPI for the excised thymus was normalized to the MPI for the heart tissue. Mean \pm SEM. $N = 4$. * $P < 0.01$, ** $P < 0.0001$. **b** Accumulation of PSS-794 in the excised thymi depends on the dexamethasone dose size. Ex vivo fluorescence images and quantification of MPI were performed 42 h after treatment with dexamethasone. Mean \pm SEM. $n = 4$. * $P < 0.05$, ** $P < 0.005$, *** $P < 0.001$

Fig. 3 Fluorescence microscopy of thymus histological sections from rats that were treated or not treated with dexamethasone. Rats were treated with dexamethasone (50 mg/kg) and sacrificed 42 h later, with a dose of either PSS-794 (a) or 794-Control (b) delivered at 24 h before sacrifice. Rats not treated with dexamethasone (No Dex) were dosed with either PSS-794 or 794-Control (3.0 mg/kg) and sacrificed 24 h later. The 10 μ m thick sections were counterstained with DAPI and anti-caspase-3 antibody. The near-infrared (NIR) image in a shows PSS-794 targeting regions of tissue containing high levels of caspase-3 due to dexamethasone treatment, whereas, the NIR image in b shows negligible accumulation of 794-Control. Scale bar = 200 μ m



Increased accumulation of PSS-794 in tumors after radiation treatment

PAIII prostate adenocarcinoma cells, taken from the same parent culture, were injected subcutaneously into both rear flanks of a cohort of syngeneic Lobund-Wistar rats [44]. After 6 days, the implanted cells had developed into two palpable tumors of similar size. With each animal, the right side tumor was treated with 20 Gy of focal beam radiation while the other tumor served as the non-treated control. 17 h after radiation, each rat was injected intravenously with either PSS-794 or 794-Control and 24 h later it was anesthetized and imaged using a planar, whole-body epifluorescence scanner. Immediately after live animal imaging, each rat was euthanized and imaged again with the skin removed from the lower region. The live animal images showed qualitatively that there was enhanced PSS-794 uptake in the radiation-treated tumor (Fig. 6a). However, quantitative interpretation of these images was difficult because, (a) the tumor signals were attenuated and diffuse due to absorption and scattering of the light by

surrounding skin and tissue, an effect that varies substantially with tumor tissue depth, and (b) PSS-794 also accumulated in the dead skin cells overlaying the treated tumor. These obfuscating factors were eliminated by imaging the rats post-mortem with the skin peeled away from the tumors. As shown by the images in Fig. 6b, there was significantly higher uptake of PSS-794 in the radiation-treated tumor relative to the non-treated tumor. In contrast, an identical study using 794-Control showed only accumulation in the kidneys and no uptake in either tumor (Fig. 6d). To evaluate the biodistribution of PSS-794, the internal organs and tissues were removed and imaged using the same near-infrared filter set. The ex vivo fluorescence imaging data in Fig. 7a confirms the high selectivity of PSS-794 for the radiation-treated tumor compared to the non-treated tumor. MPIs were quantified by taking ROI pixel intensity measurements for each tissue, and shown in Fig. 7b is a bar graph comparing PSS-794 fluorescence MPI in each tissue relative to the heart, which serves as an anatomical control. The amount of PSS-794 in the radiation-treated tumor was almost twice that in the non-treated

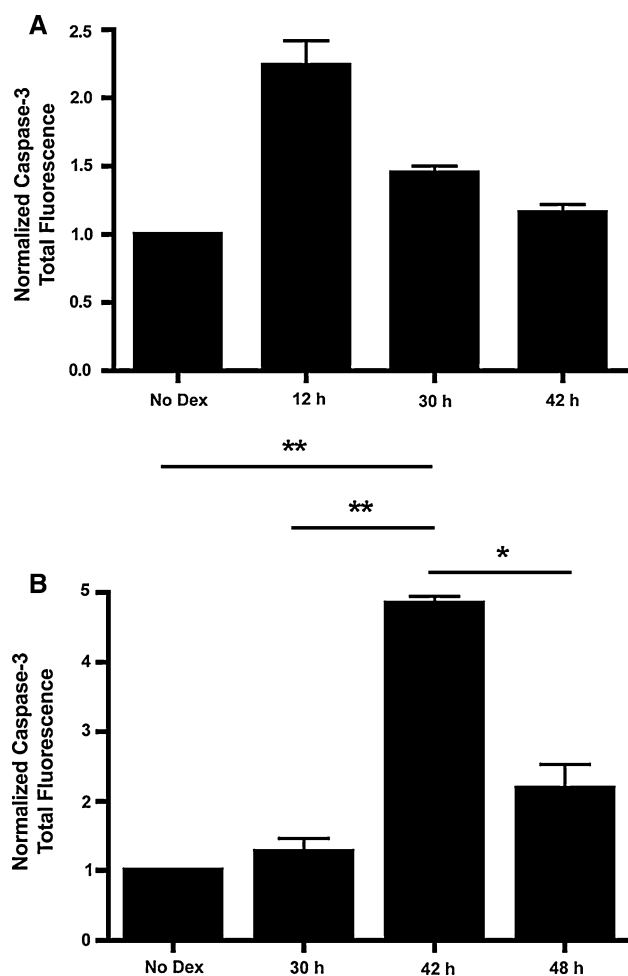


Fig. 4 Histological quantification of caspase-3 levels in rat thymus sections. **a** Rats were treated with dexamethasone (50 mg/kg) for the indicated times then sacrificed. **b** Rats treated with dexamethasone (50 mg/kg) for the indicated times and dosed with PSS-794 (3.0 mg/kg). The times in **b** indicate the period from dexamethasone treatment to sacrifice and include dosing of PSS-794 24 h before sacrifice. Rats not treated with dexamethasone (No Dex) in **b** were dosed with PSS-794 and sacrificed 24 h after probe injection. * $P < 0.01$, ** $P < 0.0001$

tumor (11.3 ± 0.2 vs. 6.5 ± 0.8 ; MPI \pm SEM) and approximately 8 fold higher than the amount of 794-Control in a treated tumor (11.3 ± 0.2 vs. 1.4 ± 0.2 ; MPI \pm SEM). Furthermore, uptake of 794-Control in the radiation-treated tumor was the same as the non-treated tumor (1.4 ± 0.2 vs. 1.4 ± 0.1 ; MPI \pm SEM). PSS-794 also accumulated in the liver, kidneys, and lungs, as seen in tumor bearing rats that were not treated with radiation. Probe signal in the liver and kidneys is not surprising since they are the clearance organs, but we presently do not have an explanation for the moderate levels of PSS-794 in the lungs. The relatively high accumulation in the skin is attributed to the localized cell death since the skin sample was taken from the area receiving focal radiation.

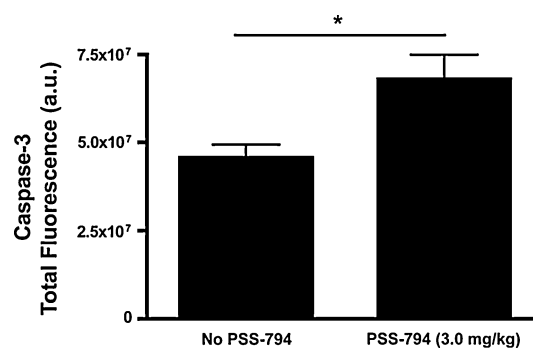


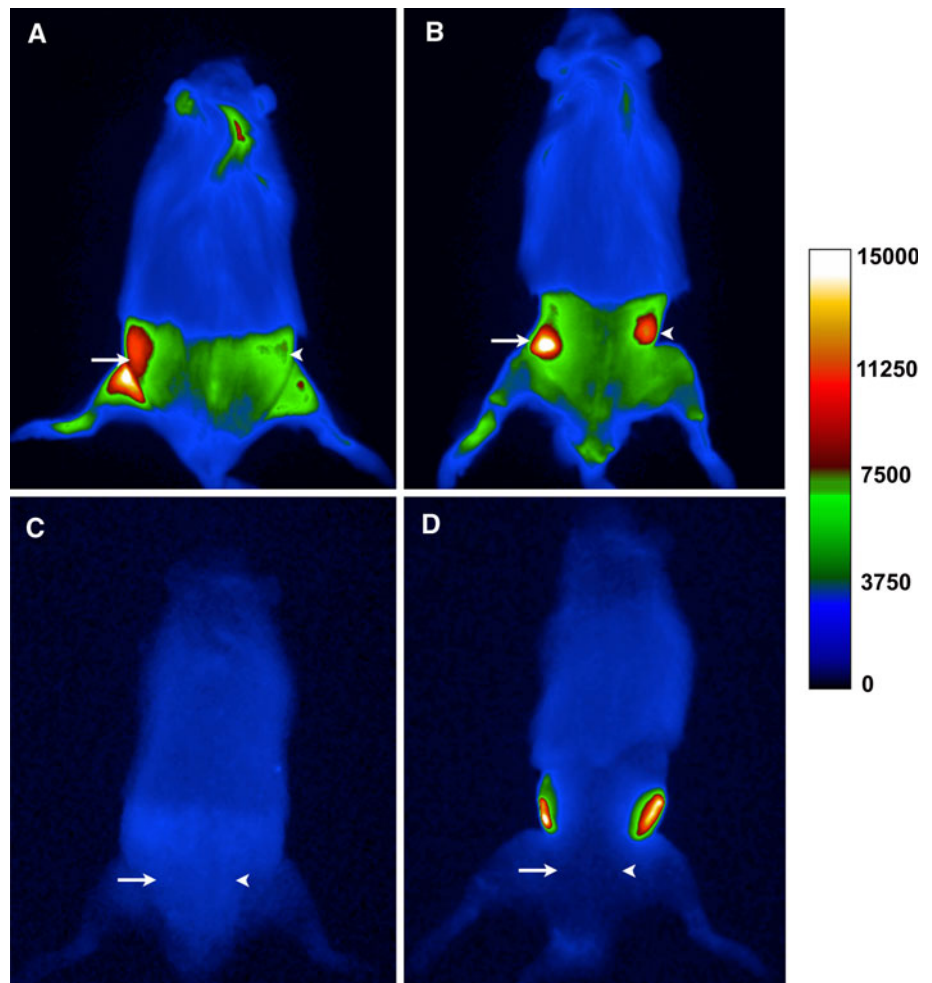
Fig. 5 Comparison of caspase-3 levels in healthy thymus tissues taken from rats either dosed or not dosed with PSS-794 (3.0 mg/kg). Two cohorts of rats were intravenously injected or not injected with PSS-794 then sacrificed after 24 h. The thymus tissues were excised, flash frozen, and cut into 10 μ m thick sections that were stained with anti-caspase-3 antibody. * $P < 0.05$

Discussion

This study examined two in vivo models of cell death that operate by distinctly different mechanisms and in different anatomical locations, thus testing the generality of the fluorescent molecular probe, PSS-794, to identify cell death in a living animal. Targeting performance was assessed by direct comparison to the untargeted fluorophore, 794-Control, that lacks a Zn^{2+} -DPA affinity unit. The first animal model treated Lobund-Wistar rats with the glucocorticosteroid dexamethasone, which induces extensive thymocyte cell death. This is a classic experimental model that is technically straightforward to conduct and has high animal throughput [47–50]. Furthermore, the kinetics for thymocyte apoptosis are well characterized and the model has been used to validate other cell death imaging probes including Annexin V [46, 51]. Ex vivo imaging and histology confirmed specific targeting of PSS-794 to the dead and dying cells in the thymus tissues (Fig. 2, 3). In contrast, negligible accumulation of the control fluorophore, 794-Control, was seen in the thymi of dexamethasone-treated rats. Increasing the dexamethasone dosage produced concomitantly higher PSS-794 accumulation in the thymus (Fig. 2b), providing further evidence that PSS-794 is targeting cell death. While the histology data show that PSS-794 stains regions of tissue sections that are high in caspase-3, the colocalization is not perfect. This is expected since the timing of caspase-3 expression during apoptosis does not coincide exactly with appearance of the PS that is targeted by PSS-794 [52, 53].

The caspase-3 histology data in Fig. 4 indicates that the number of dead and dying thymocytes in the rats treated with dexamethasone rose with time to a peak value and then declined back to the basal level. The time point for maximum caspase-3 level is determined by two competing pathways; the rate of cell death induced by the

Fig. 6 Representative planar, epifluorescence images of rats bearing two subcutaneous P4III prostate tumors and dosed with PSS-794 (**a** in vivo, **b** ex vivo) or 794-Control (**c** in vivo, **d** ex vivo) after radiation therapy. The right flank tumor (*arrow*) received focal beam radiation therapy, and the left flank tumor (*arrow head*) was not treated. At 17 h after radiation, each rat was injected intravenously with probe (3.0 mg/kg), and 24 h later the in vivo image was acquired. The rats were then sacrificed, the lower body skin removed, and the ex vivo image was acquired. The 794-Control does not target the tumors but accumulates in the kidneys. $n = 5$



dexamethasone treatment and the rate of dead cell clearance by the animal's immune response. A comparison of Fig. 4a, b shows that the presence of PSS-794 extends the time point for peak amount of caspase-3 from about 12 h after dexamethasone treatment (a time point that is similar to other kinetic studies in the literature [46]) to about 42 h. Furthermore, the basal level of dead and dying thymocytes in rats that were not treated with dexamethasone increased by about 50% when the rats were dosed with PSS-794 (Fig. 5). Thus, the presence of PSS-794 is either inducing an increase in the amount of thymocyte cell death or decreasing the rate of dead cell clearance. Our previous studies of Zn^{2+} -DPA probes have produced no evidence for cell toxicity, so it seems more likely that PSS-794 is inhibiting cell clearance. It is well-known that the appearance of PS on the cell surface is a biomarker that triggers recognition and subsequent cell clearance by phagocytes [54]. Furthermore, it is reported that the presence of PS-binding Annexin V can inhibit phagocytosis in vivo [15]. Therefore, PSS-794 may be acting like Annexin V and inhibiting dead cell clearance from the thymus by binding to PS and preventing recognition by phagocytes

[55, 56]. Future studies will attempt to confirm this explanation and address its implications. In terms of diagnostic imaging it may mean that, in certain circumstances, lower probe doses have to be employed to avoid triggering a physiological effect. However, from a therapeutic perspective, PS-binding molecules that can modulate the immune response to dead and dying cells may have value as potential anticancer agents [56].

A second, more clinically relevant animal model to evaluate the performance of PSS-794 used focal beam radiation to induce anti-tumor cell death. A rat model was generated having two subcutaneously implanted, syngeneic prostate tumors on each flank—one tumor was treated with beam radiation while the other tumor served as a non-treated control. The main advantage gained by having the experimental and control tumors on the same animal is a reduction in animal-to-animal variability. The whole-body epifluorescence images in Fig. 6 and the ex vivo organ distribution data in Fig. 7 show that PSS-794 accumulation in the radiation-treated tumor was almost double that in the non-treated tumor. Histological analyses have shown that PSS-794 targets the dead and dying tumor cells, and probe

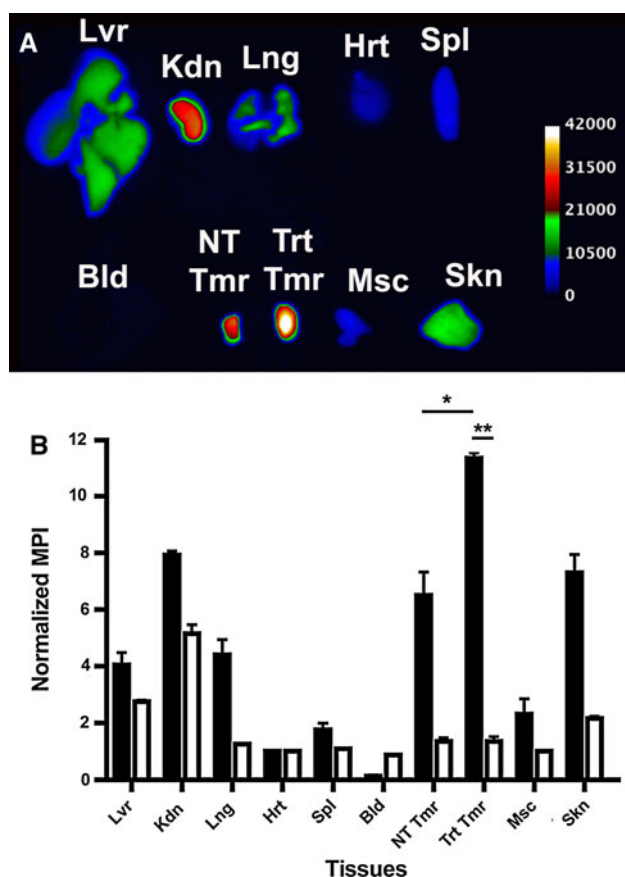


Fig. 7 Probe biodistribution in PAIII tumor bearing rats that received anti-tumor focal beam radiation. **a** Representative ex vivo fluorescence images of tissues excised from tumor-bearing rats treated with radiation therapy, dosed with PSS-794 (3.0 mg/kg) and sacrificed 24 h later. Tissues are the following: liver (Lvr), kidney (Kdn), lungs (Lng), heart (Hrt), spleen (Spl), blood (Bld), non-treated tumor (NT Tmr), radiation-treated tumor (Trt Tmr) muscle (Msc), and skin (Skn). **b** Bar graph showing ex vivo tissue distribution of PSS-794 (black bars) and 794-Control (white bars). A region of interest was drawn around each tissue and the mean pixel intensity (MPI) was recorded. The MPI from the tissues were normalized to the MPI from the heart tissue. MPI \pm SEM. $n = 5$. * $P < 0.01$, ** $P < 0.0001$

uptake in the control tumor is due to the moderately high level of necrotic tissue in this rapidly growing subcutaneous tumor model [44].

Monitoring PS externalization appears to be an objective way of assessing the level of therapy-induced tumor cell death [57–60]; thus, a reliable and robust molecular probe for exposed PS is likely to expedite anticancer research and improve the clinical decision-making process [61]. Our results indicate that Zn^{2+} -DPA probes have great promise as targeting agents for detecting increased tumor cell death due to successful therapy. However, this study also demonstrates some practical limitations with planar epifluorescence imaging using PSS-794. Although the probe has an appended near-infrared fluorophore for maximum penetration of light through skin and tissue, it is important to

realize that the penetration depth in rats is only a few millimeters and the signal intensity is highly surface weighted [62]. Thus, in vivo epifluorescence imaging using living rats is restricted to superficial tumor sites with the realistic expectation of semi-quantitative information. While it is possible to envision useful clinical applications of PSS-794 as a fluorescent probe for cell death, especially in the emerging field of fluorescence guided surgery [63], broader practical impact will be gained using imaging probes with deeper tissue penetration. For example, it should be possible to develop radiolabeled Zn^{2+} -DPA probes with sufficiently favorable pharmacokinetic profiles and high PS-affinities for microdosing and nuclear imaging.

In summary, the results of this study add to the growing evidence that the synthetic fluorescent molecular probe, PSS-794, is able to target dead and dying cells in various animal models of cell death [44, 45]. The importance of the Zn^{2+} -DPA unit as a targeting group for exposed PS on the surface of the dead and dying cells is highlighted by the lack of measurable uptake with the control dye, 794-Control. PSS-794 may become a useful optical probe for pre-clinical research efforts that aim to discover and assess new methods of anticancer treatment. It may even be possible to develop clinically useful early detection and intra-operative methods to assess cell death using surface or endoscopic optical imaging technologies.

Acknowledgments We thank Sarah Chapman for preparing the histology sections, and Chelsea Poschar and Samantha Korda for assistance in operating the accelerator. This work was supported by the Walther Cancer Foundation, the Notre Dame Integrated Imaging Facility, and NIH Grants R01GM059078 (B.D.S.), T32GM075762 (B.A.S.).

References

- Boon MJ, Smith BD (2002) Chemical control of phospholipid distribution across bilayer membranes. *Med Res Rev* 22:251–281
- Weihua Z, Tsan R, Schroit AJ et al (2005) Apoptotic cells initiate endothelial cell sprouting via electrostatic signaling. *Cancer Res* 65:11529–11535
- Yeung T, Gilbert GE, Shi J et al (2008) Membrane phosphatidylserine regulates surface charge and protein localization. *Science* 319:210–213
- Teoh NC, Ito Y, Field J et al (2007) Diannexin, a novel annexin V homodimer, provides prolonged protection against hepatic ischemia-reperfusion injury in mice. *Gastroenterology* 133:632–646
- Soares MM, King SW, Thorpe PE (2008) Targeting inside-out phosphatidylserine as a therapeutic strategy for viral diseases. *Nat Med* 14:1357–1362
- He J, Yin Y, Luster TA et al (2009) Antiphosphatidylserine antibody combined with irradiation damages tumor blood vessels and induces tumor immunity in a rat model of glioblastoma. *Clin Cancer Res* 15:6871–6880
- Thorpe PE (2010) Targeting anionic phospholipids on tumor blood vessels and tumor cells. *Thromb Res* 125:5134–5137

8. Radermacher KA, Boutry S, Laurent S et al (2010) Iron oxide particles covered with hexapeptides targeted at phosphatidylserine as MR biomarkers of tumor cell death. *Contrast Media Mol Imaging* 5:258–267
9. Kenis H, Hofstra L, Reutelingsperger CPM (2007) Annexin V: shifting from a diagnostic towards a therapeutic realm. *Cell Mol Life Sci* 64:2859–2862
10. Ran S, He J, Huang X et al (2005) Antitumor effects of a monoclonal antibody that binds anionic phospholipids on the surface of tumor blood vessels in mice. *Clin Cancer Res* 11:1551–1562
11. Weiss EM, Frey B, Rodel F et al (2010) Ex vivo- and in vivo-induced dead tumor cells as modulators of antitumor responses. *Ann NY Acad Sci* 1209:109–117
12. Krysko DV, Vandenabeele P (2008) From regulation of dying cell engulfment to development of anticancer therapy. *Cell Death Differ* 15:29–38
13. Niu G, Chen X (2010) Apoptosis imaging: beyond annexin V. *J Nucl Med* 51:1659–1662
14. Munoz LE, Franz S, Pausch F et al (2007) The influence on the immunomodulatory effects of dying and dead cells of annexin V. *J Leukocyte Biol* 81:6–14
15. Okada H, Mak TW (2004) Pathways of apoptotic and non-apoptotic death in tumor cells. *Nat Rev Cancer* 4:592–603
16. Krysko O, de Ridder L, Cornelissen M (2004) Phosphatidylserine exposure during early primary necrosis (oncosis) in JB6 cells as evidenced by immunogold labeling technique. *Apoptosis* 9:495–500
17. Degtarev A, Yuan J (2008) Expansion and evolution of cell death programmes. *Nat Rev Mol Cell Biol* 9:378–390
18. Marx J (2006) Autophagy: is it cancer's friend or foe? *Science* 312:1160–1161
19. van Delft MF, Smith DP, Lahoud MH et al (2010) Apoptosis and non-inflammatory phagocytosis can be induced by mitochondrial damage without caspases. *Cell Death Differ* 17:821–832
20. Schutters K, Reutelingsperger CPM (2010) Phosphatidylserine targeting for diagnosis and treatment of human diseases. *Apoptosis* 15:172–182
21. Boersma HH, Kietselaer BL, Stolk LM et al (2005) Past, present, and future of annexin A5: from protein discovery to clinical applications. *J Nucl Med* 46:2035–2050
22. Smith G, Nguyen Q-D, Aboagye EO (2009) Translational imaging of apoptosis. *Anti-Cancer Agent Med Chem* 9:958–967
23. Zhao M (2009) In vivo apoptosis imaging agents and strategies. *Anti-Cancer Agent Med Chem* 9:1018–1023
24. Faust A, Herman S, Wagner S et al (2009) Molecular imaging of apoptosis in vivo with scintigraphic and optical biomarkers—a status report. *Anti-Cancer Agent Med Chem* 9:968–985
25. Beekman CAC, Buckle T, van Leeuwen AC et al (2011) Questioning the value of 99 mTc-HYNIC-annexin V based response monitoring after docetaxel treatment in a mouse model for hereditary breast cancer. *Appl Radiat Isot* 69:656–662
26. Vanderheyden JL, Liu GZ, He J et al (2006) Evaluation of Tc-99 m-MAG(3)-annexin V: influence of the chelate on in vitro and in vivo properties in mice. *Nucl Med Biol* 33:135–144
27. Smith C, Mehta R, Gibson DF et al (2010) Characterization of a recombinant form of annexin VI for detection of apoptosis. *Bioconjugate Chem* 21:1554–1558
28. Waehrens LN, Heegaard CW, Gilbert GE et al (2009) Bovine lactadherin as a calcium-independent imaging agent of phosphatidylserine expressed in the surface of apoptotic HeLa cells. *Histochem Cytochem* 57:907–914
29. Krishnan AS, Neves AA, de Backer MM et al (2008) Detection of cell death in tumors by using MR imaging and a gadolinium-based targeted contrast agent. *Radiology* 246:854–862
30. Alam IS, Neves AA, Witney TH et al (2010) Comparison of the C2A domain of synaptotagmin-I and annexin-V as probes for detecting cell death. *Bioconjugate Chem* 21:884–891
31. Thapa N, Kim S, So I et al (2008) Discovery of a phosphatidylserine-recognizing peptide and its utility in molecular imaging of tumour apoptosis. *J Cell Mol Med* 12:1649–1660
32. Xiong C, Brewer K, Song S et al (2011) Peptide-based imaging agents targeting phosphatidylserine for the detection of apoptosis. *J Med Chem* 54:1825–1835
33. Laumonier C, Segers J, Laurent S et al (2006) A new peptidic vector for molecular imaging of apoptosis identified by phage display technology. *J Biomol Screen* 11:537–545
34. Burtea C, Laurent S, Lancelot E et al (2009) Peptide targeting of phosphatidylserine for the MRI detection of apoptosis in atherosclerotic plaques. *Mol Pharmaceutics* 6:1903–1919
35. Hanshaw RG, Smith BD (2005) New reagents for phosphatidylserine recognition and detection of apoptosis. *Bioorg Med Chem* 13:5035–5042
36. Koulov AV, Hanshaw RG, Stucker KA et al (2005) Biophysical studies of a synthetic mimic of the apoptosis-detecting protein annexin V. *Isr J Chem* 45:373–379
37. O'Neil EJ, Smith BD (2006) Anion recognition using dimetallic coordination complexes. *Coord Chem Rev* 250:3068–3080
38. Meers P, Mealy T (1993) Calcium-dependent annexin V binding to phospholipids: stoichiometry, specificity, and the role of negative charge. *Biochemistry* 32:11711–11721
39. Swairjo MA, Concha NO, Kaetzel MA et al (1995) Ca²⁺-binding mechanism and phospholipid head group recognition in the membrane-binding protein annexin V. *Nat Struct Biol* 2:968–974
40. Tait JF, Gibson DF, Smith C (2004) Measurement of the affinity and cooperativity of annexin V- membrane binding under conditions of low membrane occupancy. *Anal Biochem* 329:112–119
41. Leevy WM, Gammon ST, Jiang H et al (2006) Optical imaging of bacterial infection in living mice using a fluorescent near-infrared molecular probe. *J Am Chem Soc* 128:16476–16477
42. Leevy WM, Gammon ST, Johnson JR et al (2008) Non-invasive optical imaging of Staphylococcus aureus bacterial infection in living mice using a bis-dipicolylamine-zinc(II) affinity group conjugated to a near infrared fluorophore. *Bioconjugate Chem* 19:686–692
43. Smith BA, Akers WJ, Leevy WM et al (2010) Optical imaging of mammary and prostate tumors in living animals using a synthetic near infrared zinc(II)-dipicolylamine probe for anionic cell surfaces. *J Am Chem Soc* 132:67–69
44. Smith BA, Gammon ST, Xiao S et al (2011) In vivo optical imaging of acute cell death using a near-infrared fluorescent zinc-dipicolylamine probe. *Mol Pharmaceutics* 8:583–590
45. Edgington LE, Berger AB, Blum G et al (2009) Noninvasive optical imaging of apoptosis by caspase-targeted activity-based probes. *Nat Med* 8:967–974
46. Sun X-M, Dinsdale D, Snowden RT et al (1992) Characterization of apoptosis in thymocytes isolated from dexamethasone-treated rats. *Biochem Pharmacol* 44:2131–2137
47. Ahmed SA, Sriranganathan N (1994) Differential effects of dexamethasone on the thymus and spleen: alterations in programmed cell death, lymphocyte subsets and activation of T cells. *Immunopharmacology* 28:55–66
48. Mann CL, Cidrowski JA (2001) Glucocorticoids regulate plasma membrane potential during rat thymocyte apoptosis in vivo and in vitro. *Endocrinology* 142:421–429
49. Ichiyoshi H, Kiyozuka Y, Kishimoto Y et al (2003) Massive telomere loss and telomerase RNA expression in dexamethasone-induced apoptosis in mouse thymocytes. *Exp Mol Pathol* 75:178–186
50. Zavitsanou K, Nguyen V, Gregurie I et al (2007) Detection of apoptotic cell death in the thymus of dexamethasone treated rats

- using [^{123}I] annexin V and in situ oligonucleotide ligation. *J Mol Histol* 38:313–319
52. Martin SJ, Finucane DM, Amarante-Mendes GP et al (1996) Phosphatidylserine externalization during CD-95 apoptosis of cells and cytoplasts requires ICE/CED-3 protease activity. *J Biol Chem* 271:28753–28756
 53. Balasubramanian K, Mirnikjoo B, Schroit AJ (2007) Regulated externalization of phosphatidylserine at the cell surface: implications for apoptosis. *J Biol Chem* 282:18357–18364
 54. Ravichandran KS, Lorenz U (2007) Engulfment of apoptotic cells: signal for a good meal. *Nat Rev Immunol* 7:964–974
 55. Krahlting S, Callahan MK, Williamson P et al (1999) Exposure of phosphatidylserine is a general feature in the phagocytosis of apoptotic lymphocytes by macrophages. *Cell Death Differ* 6:183–189
 56. Frey B, Schildkopf P, Rödel F et al (2009) Annexin A5 renders dead tumor cells immunogenic—implications for multimodal cancer therapies. *J Immunotoxicol* 6:209–216
 57. Blankenberg FG (2008) Monitoring of treatment-induced apoptosis in oncology with PET and SPECT. *Curr Pharm Design* 14:2974–2982
 58. Manning HC, Merchant NB, Foutch AC et al (2008) Molecular imaging of therapeutic response to epidermal growth factor receptor blockade in colorectal cancer. *Clin Cancer Res* 14:7413–7422
 59. Kuge Y, Zhao S, Takei T et al (2009) Molecular imaging of apoptosis with radio-labeled annexin A5 focused on the evaluation of tumor response to chemotherapy. *Anti-Cancer Agent Med Chem* 9:1003–1011
 60. De Saint-Hubert M, Wang H, Devos E et al. (2010) Preclinical imaging of therapy response using metabolic and apoptosis molecular imaging. *Mol Imaging Biol*. doi:[10.1007/s11307-010-0412-z](https://doi.org/10.1007/s11307-010-0412-z)
 61. Brindle KM (2008) New approaches for imaging tumour responses to treatment. *Nat Rev Cancer* 8:94–107
 62. Baumes JM, Gassensmith JJ, Giblin J et al (2010) Storable, thermally activated, near-infrared chemiluminescent dyes and dye-stained microparticles for optical imaging. *Nat Chem* 2:1025–1030
 63. Ohnishi S, Vanderheyden JL, Tanaka E et al (2006) Intraoperative detection of cell injury and cell death with an 800 nm near-infrared fluorescent annexin V derivative. *Am J Transplant* 6:2321–2331